PAPER

Check for updates

A gap-designed photo-reactor for high-performance photothermal methane reforming†

Hamada A. El-Naggar, Hisao Yoshida [ID] and Akira Yamamoto [ID] *

Photothermal catalysis has garnered significant attention as a potential solution to address energy scarcity. In photothermal catalysis, light irradiation directly heats the catalyst bed, inducing a localized temperature gradient. However, in methane reforming reactions such as dry reforming, the undesired reverse reaction typically proceeds in the lower temperature zone of the catalyst bed, which reduces the overall efficiency. To address this issue, we developed a novel flow-type photo-reactor composed of a quartz tube and a quartz filler welded within the tube. The narrow catalyst-filled gap was used for catalytic reaction that minimizes the temperature gradient under light irradiation. The developed reactor, termed the gap reactor, demonstrated excellent catalytic performance in photothermal dry reforming of methane (PT-DRM), achieving ~70−80% conversion of CH_4 and CO_2 over 100 hours using a SiO_2-encapsulated Co−Ni alloy catalyst previously developed by our group. Compared to the conventional quartz tube reactor with the same cross-sectional area for light absorption, the gap reactor significantly enhanced both conversion and stability. Furthermore, integrating the gap reactor with steam addition to the reaction feed successfully suppressed coke formation to only 0.6 wt% after approximately 50 hours of reaction. This study highlights the benefits of the gap reactor design in high-temperature catalytic applications up to 1000 °C.
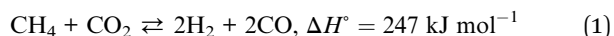
1. Introduction

Greenhouse gases (GHGs), particularly methane (CH_4) and carbon dioxide (CO_2), are recognized as major contributors to climate change, urging approaches to reduce their emissions. Dry reforming of methane (DRM, eqn (1)) is proposed to reduce both CO_2 and CH_4 emissions in an energy-intensive reaction to produce syngas. However, the highly endothermic nature of DRM and low catalyst stability present challenges. Due to the thermodynamic limitation, high CH_4 conversion could be obtained at high temperatures over 800 °C, where the temperature could be achieved by combustion of fossil fuel, similar to an industrial steam-reforming process, when constructing a large-scale process.[1,2] This dependence on fossil fuels offsets the advantages of DRM by increasing the carbon footprint of this reaction.[3] Hence, solar-induced photothermal effect was proposed to drive this reaction without the combustion of fossil fuels.[4–8]

$$CH_4 + CO_2 \rightleftarrows 2H_2 + 2CO, \Delta H° = 247 \text{ kJ mol}^{-1} \quad (1)$$

Graduate School of Human and Environmental Studies, Kyoto University, Yoshida Nihonmatsu-cho, Sakyo-ku, Kyoto 606-8501, Japan. E-mail: yamamoto.akira.2a@kyoto-u.ac.jp; Fax: +81-75-753-2988; Tel: +81-75-753-6882

† Electronic supplementary information (ESI) available. See DOI: https://doi.org/10.1039/d4se01830c
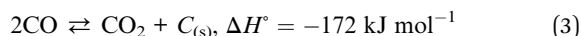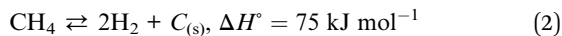
Photothermal catalysis has received significant attention due to global energy concerns. The photothermal effect can induce sufficiently high temperatures ranging from 800 to 1500 °C.[9–11] Therefore, photothermally-driven dry reforming of methane (PT-DRM) was proposed to achieve considerable CH_4 conversion.[4,12–14] However, a temperature gradient, caused by non-uniform light distribution under focused light, poses key challenges in photothermal catalysis.[4,11,15,16] This temperature gradient promotes the reverse reactions in the low-temperature zone of the catalyst bed.[15] Several recent studies have investigated reaction systems that combine external heating with photothermal catalysis,[12,17–19] these systems are likely to achieve more uniform temperature distributions. However, achieving stable and high CH_4 conversion in the PT-DRM reaction without external heating is still challenging. This raises the need for thorough studies to develop stable catalysts and optimum reactor design to maximize the CH_4 conversion under high irradiation fluxes.[4,20,21]

Temperature gradients not only decrease the conversion efficiency, but also severely compromise the catalyst stability. Although high temperatures would benefit the reaction rate and conversion in PT-DRM, they can cause significant sintering of catalytically-active metal nanoparticles.[22–25] In addition, catalysts in the low-temperature zone promote coke deposition due to the thermodynamic preference[15] via side reactions such as CH_4 decomposition (eqn (2)) and Boudouard reaction (eqn (3)).

$$CH_4 \rightleftharpoons 2H_2 + C_{(s)}, \Delta H° = 75 \text{ kJ mol}^{-1} \quad (2)$$

$$2CO \rightleftharpoons CO_2 + C_{(s)}, \Delta H° = -172 \text{ kJ mol}^{-1} \quad (3)$$

Therefore, it is crucial to develop stable catalysts with high resistances to sintering and coke deposition. We previously reported that Co–Ni alloy nanoparticles encapsulated in porous SiO_2 yolk shell (Co–Ni@SiO_2) exhibited improved activity and enhanced stability for the PT-DRM reaction, compared to the monometallic Ni@SiO_2 catalyst or impregnation catalyst without a SiO_2 shell.[15]

From the reactor design perspective, several studies have proposed new designs of photo-reactors.[5,20,21] For example, a double-tube type photo-reactor with vacuum thermal insulation and a selective solar absorbing coating was employed to achieve high temperature for CO_2 methanation under light irradiation.[26] Additionally, a reflective multi-pass photoreactor composed of a tube reactor and solar concentrator was also reported as a low-cost and highly effective photoreactor without the need for sun tracking for application under irradiation conditions.[20] These examples highlight the importance of reactor design from both fundamental and application-oriented perspectives. Inspired by these studies, we hypothesized that minimizing the temperature gradient has the potential to enhance the performance of the photothermal CH_4 reforming reaction under high-temperature conditions. Herein, we developed a novel flow-type photo-reactor consisting of a quartz tube and a quartz filler welded inside the tube, with the catalyst positioned in the gap between them (referred to hereafter as the "gap reactor", Fig. 1a). The decrease in the thickness of the catalyst layer could contribute to a decrease in the temperature gradient. The developed gap-reactor provided superior performance in CH_4 conversion through dry- and bi-reforming reactions using the Co–Ni@SiO_2 catalyst.

2. Experimental

2.1 Catalyst preparation

Co–Ni alloy nanoparticles encapsulated within a porous SiO_2 yolk shell were prepared by a two-step method according to a previous report[15] with slight modification. First, Co_5Ni_{95} hydroxide nano-platelets were prepared by hydrothermal treatment, and then encapsulated within a SiO_2 shell. Briefly, a solution of pre-dissolved polyvinylpyrrolidone (PVP, 3 g) in deionized water (DIW, 120 mL) was mixed with 0.3 mmol of $Co(NO_3)_2 \cdot 6H_2O$ and 5.7 mmol of $Ni(NO_3)_2 \cdot 6H_2O$ solutions under Ar flow. After stirring for half an hour, 30 mL of NaOH was added dropwise over 30 minutes. After that, the mixture solution was transferred to an autoclave lined with Teflon to be hydrothermally treated at 150 °C for six hours. The resulting slurry was decanted three times with DIW after it had cooled to room temperature.

After dispersing the Co_5Ni_{95} nanoplatelet suspension (150 mL), 300 mL of ethanol and 15 mL of NH_3(aq) were added. Separately, cetyltrimethylammonium bromide (CTAB, 2.7 g) was dissolved in ethanol/DIW (40 mL, 1/1, vol%). Then, 15.5 mL of tetraethyl orthosilicate (TEOS) and the CTAB solution were simultaneously added dropwise to the nanoplatelet suspension. After vigorously stirring the mixture for one hour, it settled down. After the 250 mL supernatant was decanted, the 200 mL suspension was dried at 80 °C using a water bath and then kept in an oven overnight at 80 °C to remove any remaining solvents. The catalyst was calcined at 500 °C at the heating rate of 10 °C min^{-1}.

2.2 Reactor design

A flow-type photo-reactor was designed to increase the catalyst temperature for PT-DRM effectively and minimize the temperature gradient. In this reactor, quartz fillers were welded inside
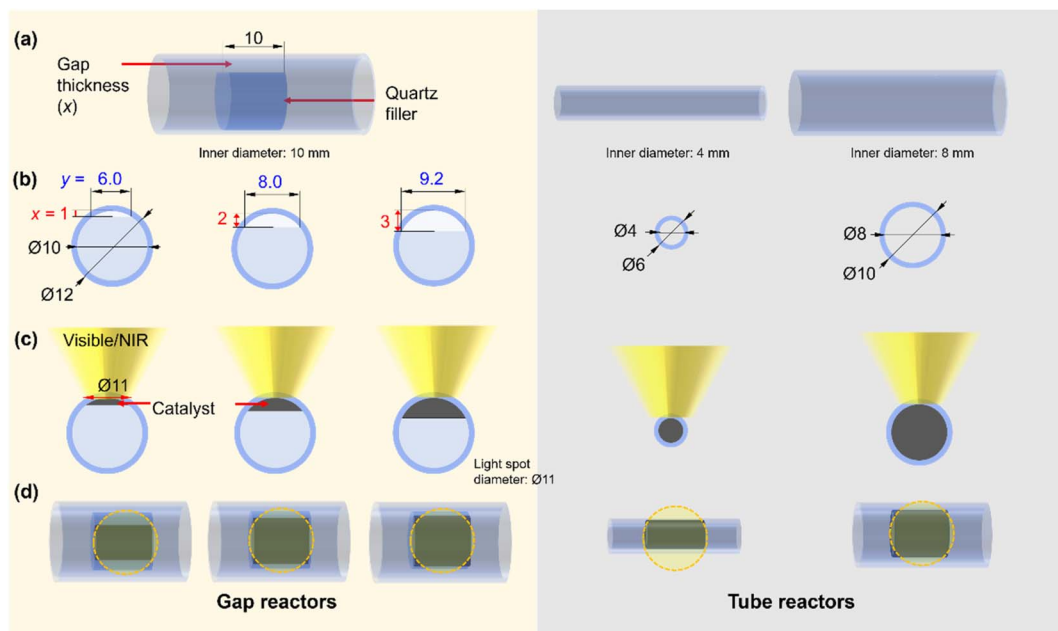

Fig. 1 Schematic representation of the photo-reactors used in this study. (a) Overview. (b) Side view. (c) Side view with catalyst. (d) Top view with catalyst. The light spot diameter of 11 mm Φ is used for the representation. Dimensions are in mm.

quartz tube reactors with an inner diameter of 10 mm, respectively (Fig. 1, for reactor's photograph please see Fig. S1†). In the flat-type quartz reactors used in our previous study,[15] controlling the thickness of the catalyst bed and light irradiation area was limited by its manufacturing process. The advantage of this gap reactor lies in its ability to regulate the catalyst space through the shape of the internal filler. In this study, three reactors with gap thicknesses of 1, 2, and 3 mm were used for catalyst filling and are referred to as x-mm-gap reactors, where x is the gap thickness. Note that, in these reactors, the cross-sectional area of the catalyst exposed to light (Fig. S2†) changes with variations in the gap thickness (Fig. 1). Moreover, the light penetration depth of the thin pellet of the reduced catalyst was <200 μm, indicating that only a limited zone at the top of the catalyst granules is directly heated by light irradiation. For the control experiments, quartz tube reactors with inner diameters of 4 and 8 mm (Fig. 1) were used, where the cross-sectional area in the 2-mm-gap reactor matchs that of the 8-mm-tube reactor. The structural information for the reactors used in this study is summarized in Table 1.

2.3 Characterization

The specific surface area was estimated from the amount of N_2 adsorption at 77 K using a BEL-MAX-G instrument (MicrotracBEL, Japan), and the porosity of the catalysts was assessed via the Barrett–Joyner–Halenda (BJH) method. X-ray diffraction (XRD) measurement was carried out at room temperature using a Shimadzu LabX XRD-6000 with Cu Kα radiation (40 kV, 30 mA). The crystallite size was determined by the Scherrer equation using the full width at half maxima (FWHM) of the diffraction line at $2\theta = 44.8°$. Transmission electron microscopy (TEM) was conducted using a JEM-2200SF and JEM-ARM200F devices (JEOL, Japan). UV-visible diffuse reflectance spectra (DRS) were recorded on a JASCO V-570 spectrophotometer with a $BaSO_4$ reference. The amount of deposited coke after the PT-DRM reaction test was determined using the elemental analysis with a CNH analyzer (MT-5 and MT-6, Yanaco Analytical Systems, Japan) and a Micro analyzer (JM-10 and JM-11, J Science Lab, Japan).

2.4 Catalytic activity tests

Photothermal and thermal catalytic activity tests were carried out under ambient pressure using a fixed-bed continuous-flow system. The powder of the $Co_5Ni_{95}@SiO_2$ catalyst was ground into 150–300 μm granules after pelletization at 40 MPa. The reactors with 1, 2, and 3-mm gap thicknesses were packed with

35, 60, and 110 mg of the granules, respectively (Table 1). The tubular reactors with inner diameters of 4 and 8 mm were filled with 60 mg and 340 mg of the catalyst granules, respectively.

Before the activity test, the catalyst was pre-treated in a 100% O_2 gas flow (5 mL min^{-1}) at 450 °C for 30 minutes to remove organics, and then reduced for 30 minutes at 600 °C using a 10% H_2/Ar gas (100 mL min^{-1}), followed by cooling to room temperature under an Ar flow. In the PT-DRM and PT-BRM reactions, gas compositions were CH_4 (22.5 mL min^{-1})/CO_2 (22.5 mL min^{-1})/N_2 (10 mL min^{-1})/Ar (145 mL min^{-1}) and CH_4 (22.5 mL min^{-1})/CO_2 (12.0 mL min^{-1})/H_2O (11.0 mL min^{-1})/N_2 (10 mL min^{-1})/Ar (145 mL min^{-1}), respectively, unless otherwise stated. A 300 W Xe lamp with a 435 nm cut-off filter and a focusing lens were used for the light irradiation. A thermal power sensor (S425C-L, Thorlabs Inc., USA) was used to measure the light power. The power (P) and diameter of the irradiated spot (Φ) were changed by altering the current of the power supply and the distance between the light source and reactor, respectively. In thermocatalytic activity tests, the catalyst was heated in a tubular electric furnace without light irradiation.

The gas products were quantified using a gas chromatograph (GC) with thermal conductivity detectors. The conversion rates of the reactants (r_x: $x = CH_4$ or CO_2) and formation rates of the products (r_y: $y = CO$ or H_2) were calculated using relative calibration factors of each gas to an internal standard of N_2. Conversion of x was obtained according to eqn (4) and (5).

$$\text{Conversion of } x \text{ (\%)} = (F_{x,\text{in}} - F_{x,\text{out}})/F_{x,\text{in}} \times 100, \quad (4)$$

where $F_{x,\text{in}}$ and $F_{x,\text{out}}$ are the flow rates of x in the inlet and outlet gases, respectively. The following equation was used to calculate the light to chemical conversion efficiency (η):

$$\eta(\%) = \left[r_{H_2}\Delta_c H^\circ_{H_2} + r_{CO}\Delta_c H^\circ_{CO} - r_{CH_4}\Delta_c H^\circ_{CH_4} \right] \Big/ P \times 100, \quad (5)$$

where $\Delta_c H^\circ_x$ and $\Delta_c H^\circ_y$ are combustion enthalpies of x or y, respectively.

The conversion and H_2/CO ratio in chemical equilibrium in the present gas compositions were calculated using the NASA CEA program.[27]

3 Results and discussion

3.1 Characterization

Fig. 2 shows the characterization results of the prepared Co–Ni@SiO$_2$ catalyst. We checked the catalyst porosity by N_2

Table 1 Information of the reactor used in this study

Reactor	Catalyst bed volume/mL	Catalyst bed length/mm	Catalyst weight/mg	GHWV^a/L g^{-1} h^{-1}
1-mm-gap	0.04	10	35	3.4×10^2
2-mm-gap	0.11	10	60	2.0×10^2
3-mm-gap	0.20	10	110	1.1×10^2
4-mm tube	0.13	10	60	2.0×10^2
8-mm tube	0.50	10	340	3.5×10^1

^{a} Gas hourly weight velocity. The total flow rate was 200 ml min^{-1}.

adsorption–desorption measurements as it was a crucial factor for the catalyst activity and stability in our previous study on PT-DRM.[15] The catalyst had a type IV isotherm as shown in Fig. 2a, and the specific surface area calculated by the BET method was 93 m^2 g^{-1}. The pore size distribution showed bimodal pore distribution around <2 nm and 10 nm (Fig. 2b). The XRD patterns of the samples after calcination and reduction pretreatments indicated that the Ni(Co)O phase with rock-salt structure was transformed to the metallic phase upon reduction at 600 °C (Fig. 2c). The crystallite size of the metallic phase was estimated to be 11.0 nm using the Scherrer equation. The spent catalyst maintained the metallic phase after the 2 h PT-DRM activity test using the 3-mm gap reactor with a slight increase of the crystallite size to around 16.1 nm. Based on the TEM images in Fig. 2d, the metal nanoparticles were encapsulated within the SiO_2 shell. The mean particle size of 13.5 nm (Fig. 2e) was consistent with the crystallite size by XRD. The diffuse reflectance spectra (Fig. 2f) showed enhanced light absorption properties upon reduction treatment.

3.2 Activity test results

3.2.1 Effect of light power. First, we investigated the effect of the gap thickness (1, 2, and 3 mm) on the catalytic performance at the light spot diameter of 11 mm under various light power conditions. For all gap thicknesses, the surface temperature of the reactor and formation rates of H_2 and CO (r_{H_2} and r_{CO}) increased with the increase in light power (Fig. 3a and b). A similar trend was observed in our previous study on thermal and photothermal DRM reactions,[15] where increased reaction temperature typically enhances the catalytic performance. The 2-mm-gap reactor showed higher r_{CO} and r_{H_2} values at all light power values (18–25 W) compared to the 1-mm-gap and 3-mm-gap reactors. The surface temperature of the reactor increased

with the gap thickness from 1 to 2 mm, likely due to the larger cross-sectional area of the catalyst zone available for light absorption (Fig. 1d; for details, see Fig. S2†). Notably, the 1-mm-gap reactor achieved significantly higher formation rates of H_2 and CO at a light power of 25 W even at a low surface temperature of 686 °C, compared to the 3-mm-gap reactor (surface temperature: 811 °C), as shown in Fig. 3a. These results highlight the positive effect of reducing the gap thickness. On the other hand, at a gap-thickness of 3 mm, the formation rates of H_2 and CO decreased compared to that of 2 mm despite the similar surface temperatures across all light power levels. Based on these results, we concluded that a 2-mm-gap is optimum for PT-DRM under the present reaction conditions.

Additionally, the H_2/CO ratio was lower than the stoichiometric value in DRM (i.e., 1, eqn (1), Fig. 3b, right axis). This could be interpreted by the simultaneous occurrence of side reactions such as reverse water gas shift reaction (eqn (6)).

$$CO_2 + H_2 \rightleftarrows H_2O + CO, \Delta H° = 41 \text{ kJ mol}^{-1} \quad (6)$$

Furthermore, the H_2/CO ratio increased with increasing light power in all gap reactors, although the difference was slight in the 2-mm-gap and 3-mm-gap reactors. The trend is likely attributed to the thermodynamic equilibrium because the H_2/CO ratio increases at higher temperatures (Fig. S3†). The light-to-fuel conversion efficiency (η) in the 2-mm-gap reactor was 6.0% at 25 W at the conversion range of approximately 60% (Fig. 3c, S4†).

To investigate the performance of this reactor system in the absence of light irradiation, we conducted thermal DRM activity tests using an electric furnace from 500 to 700 °C. In these tests, we used the 2-mm-gap reactor and tube reactor (inner diameter: 4 mm) without altering the catalyst amount (60 mg) and the
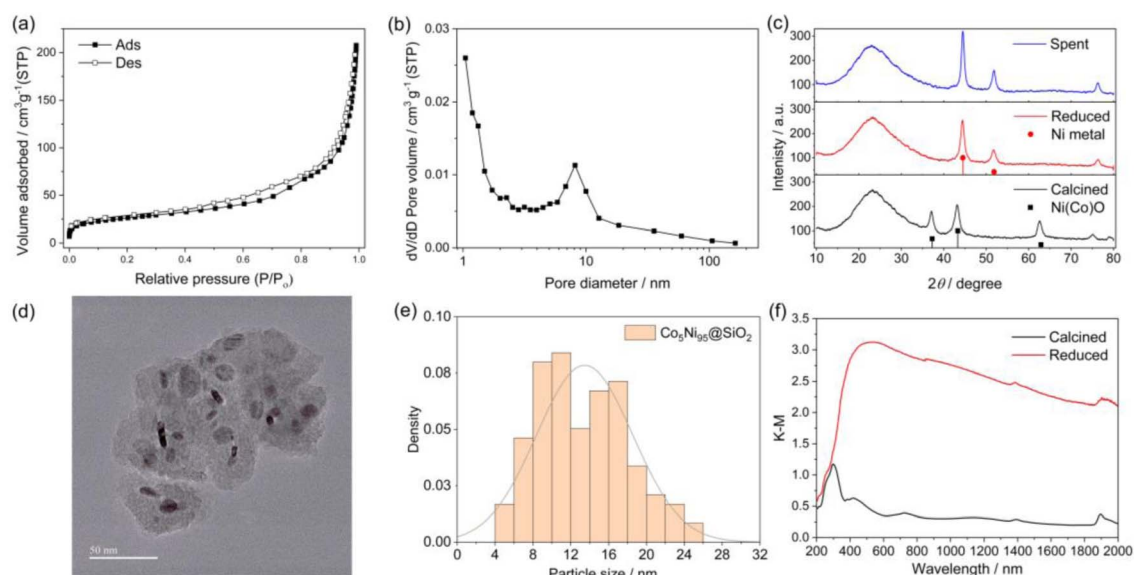

Fig. 2 Characterization results of the Co_5Ni_{95}@SiO_2 catalyst. (a) N_2 adsorption–desorption isotherm. (b) Pore size distribution of the calcined sample. (c) XRD patterns of the calcined, reduced and spent catalysts. (d and e) TEM image and particle size distribution of the reduced catalyst. The scale bar is 50 nm. (f) UV-visible DRS of the calcined and reduced catalysts.
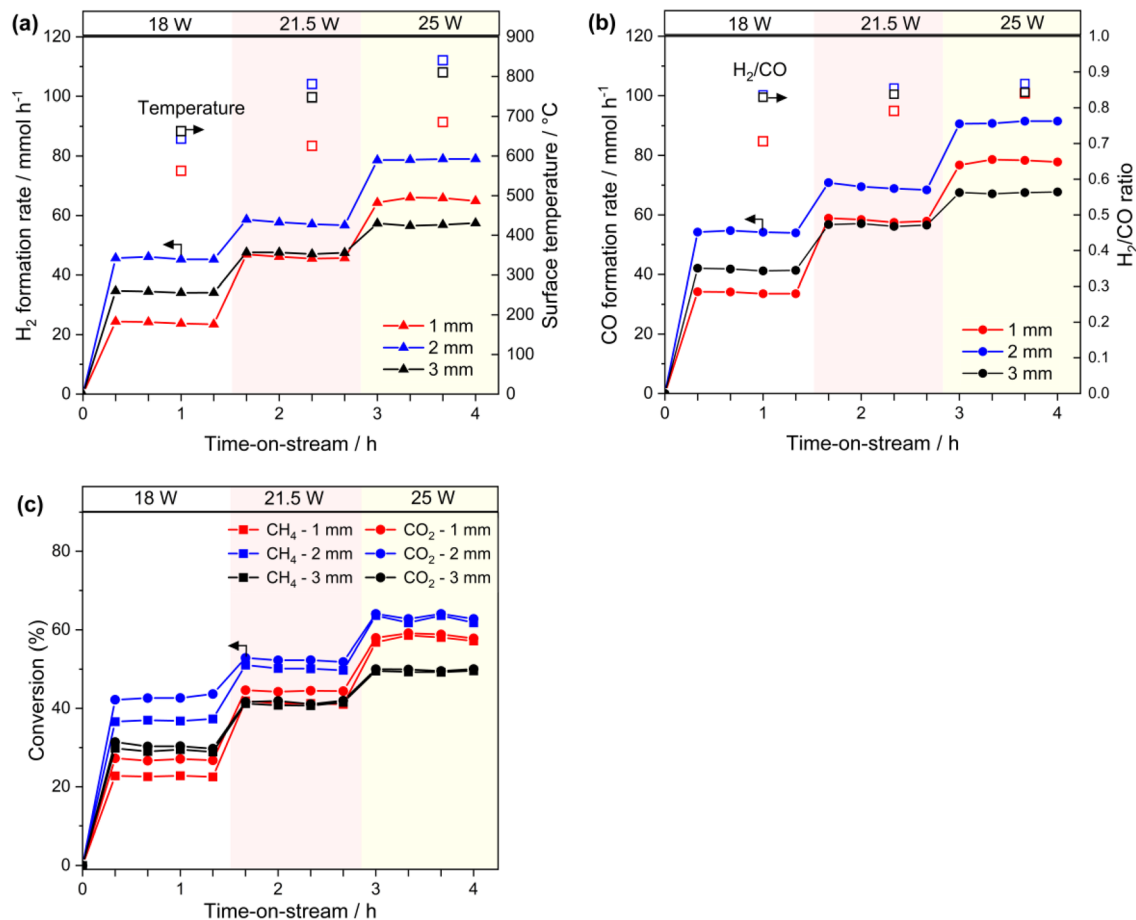
Fig. 3 Results of photothermal catalytic activity tests using 1-, 2-, and 3-mm-gap reactors (P = 18, 21.5, or 25 W, and Φ = 11 mm). (a) H_2 formation rate, (b) CO formation rate, and (c) conversion of CH_4 and CO_2.

reaction gas feed. The formation rates of H_2 and CO (Fig. 4) and conversions of CH_4 and CO_2 increased with rising the reaction temperature. Moreover, as the reaction temperature increased, the H_2/CO ratio increased, which was consistent with the photothermal activity test using the 1-mm-reactor (Fig. 3b and c, right axis) and was not observed in the 3-mm-gap reactor. This

comparison suggests that, at the increased gap thickness of 3 mm, reverse or side reactions proceeded at the lower temperature zone of the back side of the reactor.

3.2.2 Spot diameter and position. The irradiated spot diameter and position significantly affect the temperature distribution and reaction efficiency.[15,28] We investigated the
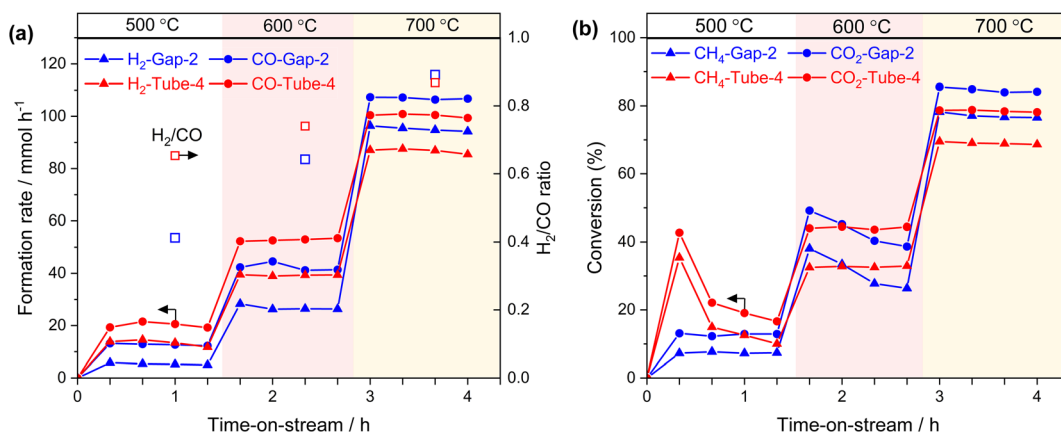

Fig. 4 Results of thermal DRM activity tests using the 2-mm-gap reactor, and 4-mm tube reactors under 500, 600, and 700 °C. (a) Formation rates of H_2 and CO, and H_2/CO (right-axis). (b) Conversion of CH_4 and CO_2.

effect of spot diameter at a light power of 25 W. The formation rates of H_2 and CO increased with decreasing the spot diameter across all gap thicknesses (Fig. 5a), accompanied by an increase in surface temperature (Fig. 5b, right axis). The results indicate that the decreased spot diameter from 11 to 7 mm (*i.e.*, increased light flux) positively influenced the performance. The cross-sectional area for the light absorption decreased from 0.76 to 0.38 cm^2 with a decrease in the spot diameter from 11 to 7 mm in the case of the 2-mm-gap reactor. Considering that the increased cross-sectional area can positively contribute to the rise in temperature, the increased temperature and performance originate from the increased light flux under the present conditions.

The impact of the temperature gradient perpendicular to the light irradiation direction on the catalytic activity was evaluated using the 2-mm gap reactor by irradiating different positions of the catalyst bed with a 7-mm-spot (Fig. 6a). Light irradiation to the middle and downstream positions resulted in slightly higher formation rates of CO and H_2 compared to the upstream irradiation (Fig. 6b). We previously reported irradiation to the downstream position produced twice the conversion and

formation rates compared with irradiating the upstream position using a flat type reactor (irradiation area: 20 mm × 20 mm, thickness: 1 mm, light spot diameter: 7 mm Φ).[15] The difference in the performance was attributed to the reverse reaction being promoted at a low-temperature downstream zone when the upstream zone was irradiated.[15] In the present experiment, the size of the irradiation area (8 mm × 10 mm, Fig. 1) was nearly consistent with the light spot diameter (7 mm Φ), which is likely to reduce the positional effect of the light spot on the catalytic activity. It is worth mentioning that the cross-sectional area of the catalyst zone in the gap reactor is easily adjusted by modifying the inner diameter of the quartz tube and the size of the inner filler. This flexibility provides a significant advantage in avoiding the mismatches of the light absorbing area and the light spot.

3.2.3 Comparison with tubular reactors in long-term reaction.

The long-term stability of the catalytic systems was examined using the 2-mm-gap reactor and tubular reactor (inner diameter: 8 mm), with catalyst amounts of 60 and 340 mg, respectively (catalyst length: 10 mm). The 2-mm-gap reactor demonstrated excellent catalytic performance of ~78%
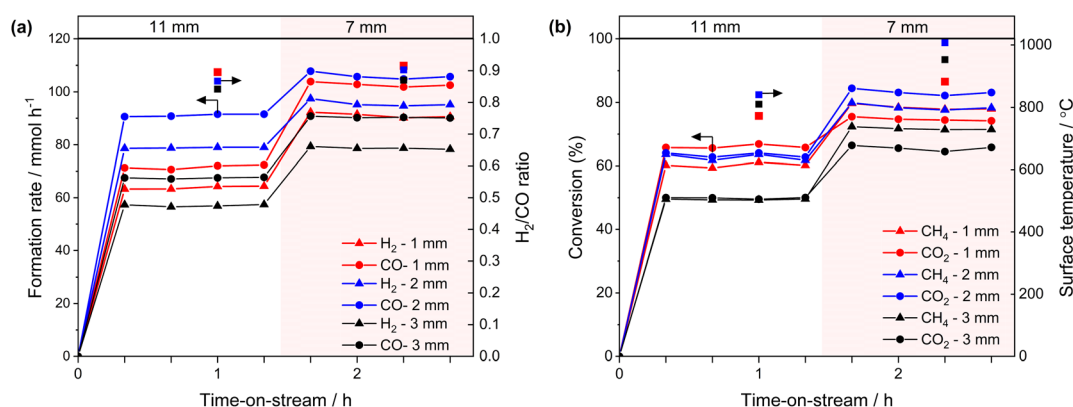

Fig. 5 Results of activity tests using 1-, 2-, and 3-mm-gap reactors ($P = 25$ W, and $\Phi = 11$ or 7 mm). (a) Formation rates of H_2 and CO, and H_2/CO (right-axis). (b) Conversion of CH_4 and CO_2, and surface temperature (right-axis).
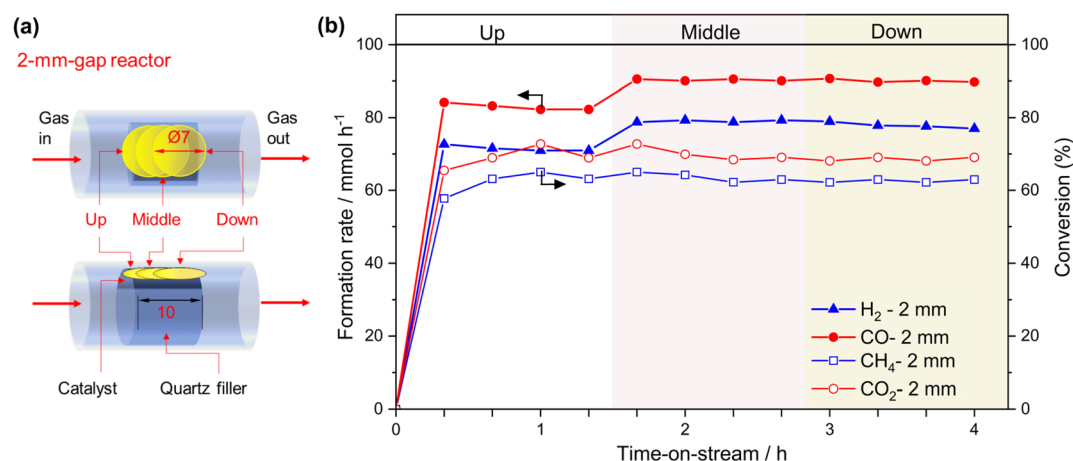

Fig. 6 Effect of the position of the light spot on the photothermal catalytic activity. (a) Schematic representation. (b) Formation rates of H_2 and CO (left-axis) and conversion (right-axis) of CH_4 and CO_2 using the 2-mm-gap reactor. ($P = 25$ W, $\Phi = 7$ mm.)

CO_2 conversion and ~72% CH_4 conversion over 100 hours during PT-DRM (Fig. 7a). The temporal decrease of the performance was observed in 10–20 hours of PT-DRM, which aligns with previously reported phenomena in thermal DRM reactions and it is likely attributed to coke deposition.[29–31] In contrast, the 8-mm-tube reactor, with the same cross-sectional area for light absorption as the 2-mm-gap reactor, exhibited significantly lower conversion levels, with ~60% for CO_2 and ~50% for CH_4 (Fig. 7b). It should be pointed out that the GHWV value in the 8-mm-tube reactor is 5.7 times lower than that in the 2-mm-gap reactor. These results emphasized the effectiveness of reducing the catalyst bed thickness to enhance performance in PT-DRM. To the best of our knowledge, the conversion level achieved in this study is the highest reported for systems utilizing a low-power light source, such as 300–500 W Xe lamps (for details please see Table S1†), without external heating.[15–17,32–37] Note that higher CH_4 conversion levels have been reported in PT-DRM when using high-power Xe lamps (e.g., 3 kW[38] or 6 kW[39]). Separately, the existence of a temperature gradient (> approximately 200 °C) was confirmed using thermocouples under a flow of inert gas, even in the case of the

2-mm-gap reactor (ESI Note 1†). These results indicate that the gap reactor mitigated the temperature gradient, resulting in high conversion even under relatively low light irradiation conditions by suppressing the reverse reaction at the low-temperature zone. Additionally, we confirmed that the conversion of CO_2 and CH_4 was approximately 60% when using the 4-mm-tube reactor (Fig. S5†), where the same catalyst amount and bed length were employed as used in the 2-mm-gap reactor.

Coke formation is one of the crucial challenges in PT-DRM. Based on elemental analysis, the amount of deposited coke after 100-hours-reaction was 17 mg (28.3 wt%) in the 2-mm-gap reactor and 115 mg (33.8 wt%) in the 8-mm tube reactor. The reduced coke formation can be attributed to the decreased temperature gradient because the coke formation is thermodynamically favorable at lower temperatures.

The addition of steam into the reaction feed in DRM (i.e., bi-reforming) is an effective strategy for reducing the coke formation and controlling the H_2/CO ratio in the produced syngas.[40,41] To check the applicability of this gap reactor, we conducted the photothermal bi-reforming of methane (PT-BRM) using a reaction feed of CH_4 (22.5 mL min^{-1})/CO_2 (12.0 mL min^{-1})/H_2O (11.0 mL min^{-1})/N_2 (10.0 mL min^{-1})/Ar (145 mL min^{-1}). In the PT-BRM test, the r_{H_2} increased significantly to over 100 mmol h^{-1} compared to the PT-DRM results (Fig. 7c). The CO_2 and CH_4 conversions were 75% and 73%, respectively, after 52 h of the activity test. The H_2/CO ratio was 1.4 under PT-BRM conditions, substantially higher than that observed under PT-DRM conditions. Furthermore, the amount of the deposited coke after 52 h was only 0.6 wt%, indicating a significant reduction of coke formation due to steam addition. These results suggest that combining the developed gap reactor with PT-BRM could pave the way for highly active and stable solar reforming systems. Additionally, this study underscores the critical role of reactor design in photothermal reactions and provides a novel method for developing efficient photo-reactors.

4. Conclusions

In photothermal dry-reforming of methane (PT-DRM), the temperature gradient induced by light irradiation poses a significant challenge, as catalysts at a low-temperature zone promote the reverse reaction, thereby reducing overall catalytic performance. This study demonstrated the effectiveness of a novel gap reactor with controllable thickness for mitigating a temperature gradient and enhancing catalytic performance in PT-DRM. Using the gap reactor, approximately 78% of CO_2 conversion and 72% of CH_4 conversion were achieved over 100 hours on the Co–Ni@SiO$_2$ catalyst developed by our group previously. Compared to the conventional tube reactors, the gap reactor exhibited substantially higher conversion and long-term stability. Furthermore, the developed gap reactor showed excellent catalytic performance for the photothermal bi-reforming of methane, with suppressed coke formation to only 0.6 wt% after approximately 50 hours of reaction. These findings highlight the potential of this novel gap reactor design for photothermal catalysis, offering a promising pathway for
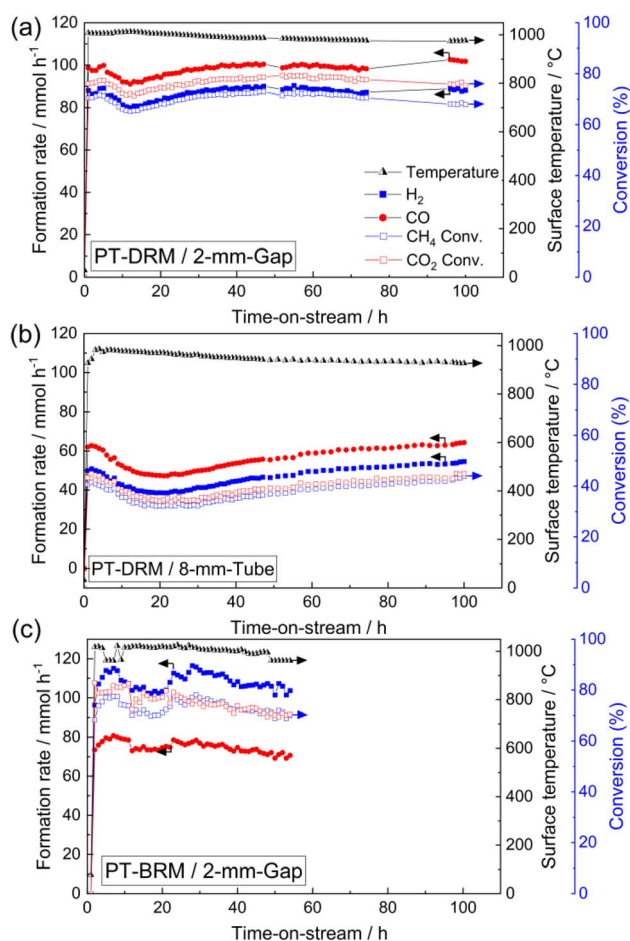
Fig. 7 Results of the long-time stability test using various reactors. (a) 2-mm gap reactor in PT-DRM. (b) 8-mm tubular in PT-DRM. (c) 2-mm gap reactor in PT-BRM. (P = 25 W, Φ = 7 mm, and spot position: middle.)

advancing catalytic reforming processes powered by solar energy.

Data availability

The authors confirm that the data supporting the findings of this study are available within the article and its ESI.†

Author contributions

H. A. E. and A. Y. conceptualized this work. H. A. E. conducted the experiments and wrote this manuscript with support from A. Y and H. Y. A. Y. supervised this project with advice from H. Y. The manuscript was written through contributions of all authors and all authors have given approval to the final version of the manuscript.

Conflicts of interest

The authors declare that a patent application (Japanese Patent Application No. 2024-192704) has been filed based on the results described in this manuscript.

Acknowledgements

References

1 T. N. From, B. Partoon, M. Rautenbach, M. Østberg, A. Bentien, K. Aasberg-Petersen and P. M. Mortensen, *Chem. Eng. J.*, 2024, **479**, 147205.

2 S. T. Wismann, J. S. Engbæk, S. B. Vendelbo, F. B. Bendixen, W. L. Eriksen, K. Aasberg-Petersen, C. Frandsen, I. Chorkendorff and P. M. Mortensen, *Science*, 2019, **364**, 756–759.

3 L. E. Sandoval-Diaz, R. Schlogl and T. Lunkenbein, *Catalysts*, 2022, **12**, 465.

4 J. Y. Y. Loh, A. Wang, A. Mohan, A. A. Tountas, A. M. Gouda, A. Tavasoli and G. A. Ozin, *Adv. Sci.*, 2024, **11**, 2306604.

5 Y. Jiang, S. Li, Y. Fan and Z. Tang, *Angew. Chem., Int. Ed.*, 2024, **63**, e202404658.

6 X. Li, C. Wang and J. Tang, *Nat. Rev. Mater.*, 2022, **7**, 617–632.

7 S. A. M. Said, M. Waseeuddin and D. S. A. Simakov, *Renewable Sustainable Energy Rev.*, 2016, **59**, 149–159.

8 E. J. Sheu, E. M. A. Mokheimer and A. F. Ghoniem, *Int. J. Hydrogen Energy*, 2015, **40**, 12929–12955.

9 M. Romero and A. Steinfeld, *Energy Environ. Sci.*, 2012, **5**, 9234–9245.

10 E. Casati, L. Allgoewer and A. Steinfeld, *Device*, 2024, **2**, 100399.

11 W. Sarwana, D. Takami, A. Yamamoto and H. Yoshida, *Catal. Sci. Technol.*, 2023, **13**, 1755–1762.

12 A. Tavasoli, A. Gouda, T. Zahringer, Y. F. Li, H. Quaid, C. J. Viasus Perez, R. Song, M. Sain and G. Ozin, *Nat. Commun.*, 2023, **14**, 1435.

13 A. Tavasoli and G. Ozin, *Joule*, 2018, **2**, 571–575.

14 X. Tian and F. Wang, *Sep. Purif. Technol.*, 2025, **354**, 128799.

15 H. A. El-Naggar, D. Takami, H. Asanuma, T. Hirata, H. Yoshida and A. Yamamoto, *ChemCatChem*, 2024, e202401396.

16 D. Takami, J. Tsubakimoto, W. Sarwana, A. Yamamoto and H. Yoshida, *ACS Appl. Energy Mater.*, 2023, **6**, 7627–7635.

17 J. Zhang, K. Xie, Y. Jiang, M. Li, X. Tan, Y. Yang, X. Zhao, L. Wang, Y. Wang, X. Wang, Y. Zhu, H. Chen, M. Wu, H. Sun and S. Wang, *ACS Catal.*, 2023, **13**, 10855–10865.

18 D. Takami, Y. Ito, S. Kawaharasaki, A. Yamamoto and H. Yoshida, *Sustainable Energy Fuels*, 2019, **3**, 2968–2971.

19 T. Xie, Z.-Y. Zhang, H.-Y. Zheng, K.-D. Xu, Z. Hu and Y. Lei, *Chem. Eng. J.*, 2022, **429**, 132507.

20 P. Kant, S. Liang, M. Rubin, G. A. Ozin and R. Dittmeyer, *Joule*, 2023, **7**, 1347–1362.

21 W. K. Fan and M. Tahir, *Chem. Eng. J.*, 2022, **427**, 131617.

22 I. V. Yentekakis, P. Panagiotopoulou and G. Artemakis, *Appl. Catal., B*, 2021, **296**, 120210.

23 H. Wu, J. Liu, H. Liu and D. He, *Fuel*, 2019, **235**, 868–877.

24 C. Wang, Y. Qiu, X. Zhang, Y. Zhang, N. Sun and Y. Zhao, *Catal. Sci. Technol.*, 2018, **8**, 4877–4890.

25 M. Yang, P. Jin, Y. Fan, C. Huang, N. Zhang, W. Weng, M. Chen and H. Wan, *Catal. Sci. Technol.*, 2015, **5**, 5095–5099.

26 Y. Li, J. Hao, H. Song, F. Zhang, X. Bai, X. Meng, H. Zhang, S. Wang, Y. Hu and J. Ye, *Nat. Commun.*, 2019, **10**, 2359.

27 B. J. McBride, *Computer Program for Calculation of Complex Chemical Equilibrium Compositions and Applications*, NASA Lewis Research Center, 1996.

28 G. Baffou, I. Bordacchini, A. Baldi and R. Quidant, *Light:Sci. Appl.*, 2020, **9**, 108.

29 T. Sukonket, A. Khan, B. Saha, H. Ibrahim, S. Tantayanon, P. Kumar and R. Idem, *Energy Fuels*, 2011, **25**, 864–877.

30 M. A. Vasiliades, P. Djinović, L. F. Davlyatova, A. Pintar and A. M. Efstathiou, *Catal. Today*, 2018, **299**, 201–211.

31 P. Djinović and A. Pintar, *Appl. Catal., B*, 2017, **206**, 675–682.

32 H. Huang, M. Mao, Q. Zhang, Y. Li, J. Bai, Y. Yang, M. Zeng and X. Zhao, *Adv. Energy Mater.*, 2018, **8**, 1702472.

33 S. Shoji, X. Peng, A. Yamaguchi, R. Watanabe, C. Fukuhara, Y. Cho, T. Yamamoto, S. Matsumura, M.-W. Yu, S. Ishii, T. Fujita, H. Abe and M. Miyauchi, *Nat. Catal.*, 2020, **3**, 148–153.

34 X. Liu, H. Shi, X. Meng, C. Sun, K. Zhang, L. Gao, Y. Ma, Z. Mu, Y. Ling, B. Cheng, Y. Li, Y. Xuan and Y. Ding, *Sol. RRL*, 2021, **5**, 2100185.

35 S. Wu, G. Ji, P. Qiu, Q. Hu, J. Tian and Y. Li, *Sol. RRL*, 2022, **6**, 2200369.

36 Z. Xie, Y. Li, Z. Zhou, Q. Hu, J. Wu and S. Wu, *J. Mater. Chem. A*, 2022, **10**, 7099–7110.

37 Z. Cui, Q. Hu, Y. Li, J. Wu, X. Yu, H. Cao, L. Ji, M. Zhong and Z. Chen, *Appl. Catal., B*, 2024, **350**, 123917.

38 T. Kodama, H. Ohtake, K. Shimizu and Y. Kitayama, *Energy Fuels*, 2002, **16**, 1016–1023.

39 T. M. Abdellateif, J. Sarwar, E. C. Vagia and K. E. Kakosimos, *Chem. Eng. J.*, 2023, **452**, 139190.

40 K. Jabbour, *J. Energy Chem.*, 2020, **48**, 54–91.

41 A. Ali Khan, M. Tahir and N. Khan, *Energy Convers. Manage.*, 2023, **286**, 117021.